

Angle-resolved photoemission spectroscopy study of $\text{HgBa}_2\text{CuO}_{4+\delta}$

I. M. Vishik,¹ N. Barišić,^{2,3} M.K. Chan,² Y. Li,^{4,5} D. D. Xia,^{2,6,*} G. Yu,² X. Zhao,^{2,6} W. S. Lee,^{7,8} W. Meevasana,⁹ T. P. Devereaux,^{7,8} M. Greven,² and Z. X. Shen^{7,8}

¹*Massachusetts Institute of Technology, Department of Physics, Cambridge, MA, 02139, USA*

²*University of Minnesota, School of Physics and Astronomy, Minneapolis, MN 55455, USA*

³*Institute of Solid State Physics, Vienna University of Technology, Vienna, 1040, Austria*

⁴*Peking University, International Center for Quantum Materials, School of Physics, Beijing, 100871, China*

⁵*Collaborative Innovation Center of Quantum Matter, Beijing, 100871, China*

⁶*State Key Laboratory of Inorganic Synthesis and Preparative Chemistry, College of Chemistry, Jilin University, Changchun, 130012, China*

⁷*Stanford Institute for Materials and Energy Sciences,*

SLAC National Accelerator Laboratory, 2575 Sand Hill Road, Menlo Park, CA 94025, USA

⁸*Geballe Laboratory for Advanced Materials, Departments of Physics*

and Applied Physics, Stanford University, Stanford, CA 94305, USA

⁹*Suranaree University of Technology, School of Physics, Muang, Nakhon Ratchasima, 30000, Thailand*

(Dated: February 11, 2014)

$\text{HgBa}_2\text{CuO}_{4+\delta}$ (Hg1201) has been shown to be a model cuprate for scattering, optical, and transport experiments, but angle-resolved photoemission spectroscopy (ARPES) data are still lacking owing to the absence of a charge-neutral cleavage plane. We report on progress in achieving the experimental conditions for which quasiparticles can be observed in the near-nodal region of the Fermi surface. The d -wave superconducting gap is measured and found to have a maximum of 39 meV. At low temperature, a kink is detected in the nodal dispersion at approximately 51 meV below the Fermi level, an energy that is different from other cuprates with comparable T_c . The superconducting gap, Fermi surface, and nodal band renormalization measured here provide a crucial momentum-space complement to other experimental probes.

Hg1201 is a cuprate whose structural simplicity and low residual resistivity makes it an ideal compound for many experiments including charge transport¹, Raman^{2,3}, NMR⁴, thermodynamics⁵⁻⁷, and neutron⁸ and x-ray scattering^{9,10}. It has a simple tetragonal single-layer crystal structure (P4/mmm), and oxygen dopants reside in the Hg layer, relatively far from the CuO_2 planes, minimizing disorder effects^{11,12}. In fact, it is a model cuprate for gaining quantitative information from transport and optical measurements^{1,12-15}. Additionally, quantum oscillations have recently been reported in underdoped Hg1201, attesting to the long mean free path and confirming the universality of small Fermi pockets in the field-induced resistive state¹⁶. The highest superconducting T_c was reported in a related triple-layer compound¹⁷, so in addition to offering general insight on the cuprates, the study of Hg1201 may provide a perspective on how to maximize T_c ¹⁸.

However, there have not yet been peer reviewed ARPES studies of Hg1201 in the literature. The reason for this is that the cleaved surfaces are not ideal, which makes it difficult to obtain useful spectra. Here, we present the progress we have made in obtaining the optimal experimental conditions to study Hg1201 with ARPES, which allowed us to quantitatively measure the near-nodal electronic structure of this material. We find that data quality strongly hinges on selecting the proper experimental conditions. With the experiment optimized to achieve the sharpest near-nodal spectra, we are able to estimate the Luttinger volume, measure the d -wave superconducting gap near the node, and observe a nodal

renormalization feature near 50 meV.

I. EXPERIMENTAL CONDITIONS

The schematic crystal structure of Hg1201 is shown in Fig. 1(a). It can be seen that the structure lacks a neutral cleavage plane, as there is nowhere to slice the unit cell in a fashion that would yield identical atomic planes on both sides of the cleave. Additionally, the Hg1201 crystal structure, adjacent layers have opposite charges (Fig. 1(b)), so any pure termination would produce a polar catastrophe¹⁹ (electric potential increasing to infinity) which must be mitigated either by self-doping or by a mixed-termination. Scanning surface microscopies of Hg1201 have indicated that the topography of cleaved surfaces consists of 4nm step edges with flat terraces extending hundreds of nanometers²⁰. Core level x-ray photoelectron spectroscopy (XPS) suggests that the surface termination is near the Hg layer because the Hg:Cu and Hg:Ba intensity ratios normalized by the XPS sensitivity to those elements was larger than expected from the chemical formula²¹.

Single crystals were grown by the two-step flux method by which a maximum T_c onset of 96.5K can be achieved²². In preparing Hg1201 samples for ARPES experiments, care was taken to ensure electrical conductance between the sample and the sample post. Samples were glued onto the copper sample post using EPO-TEK H21D silver epoxy (Epoxy technology Inc). While this silver epoxy provides adequate conduction between the

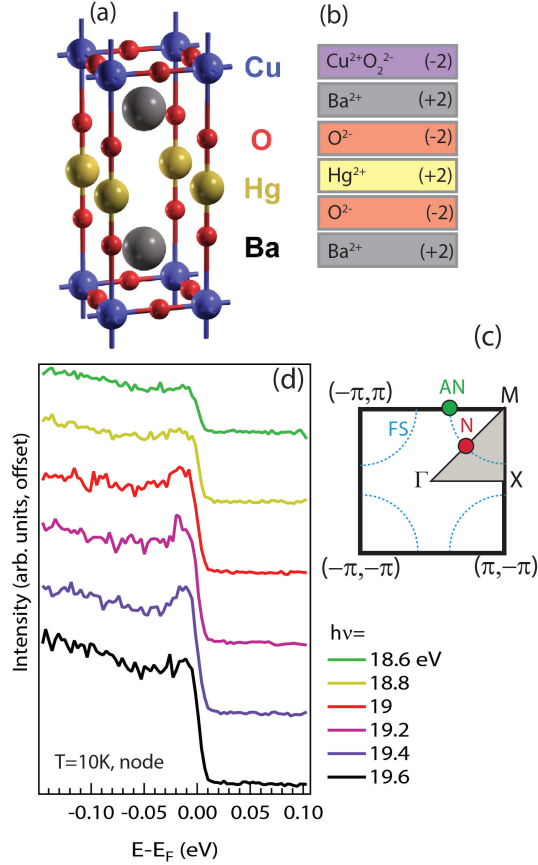


FIG. 1. (a) Schematic crystal structure of Hg1201 for simplicity drawn without oxygen interstitials in the Hg layers (top). Image from Ref. 1. (b) charges of each layer in the crystal structure, excluding oxygen interstitials. (c) 2D projection of tetragonal Brillouin zone (BZ) with high symmetry points labeled. Schematic of Fermi surface (FS) is shown by blue dashed lines. Red dot marks the nodal (N) momentum, where the Fermi surface intersects the BZ diagonal $((0,0)-(\pi,\pi)$ line), and green dot marks the antinodal (AN) momentum, where the FS intersects the BZ boundary. (d) Photon energy dependence of EDCs at nodal momentum (red dot in (c)). Data taken on a single sample at SSRL with cuts along BZ diagonal.

copper post and most compounds, Hg1201 samples were not found to be properly grounded to the post after this step. This may be due to the epoxy reacting with the Hg1201 surface. Thus, the silver epoxy provides only mechanical adhesion in our experiments. For conduction, silver paint (Dupont 4299N) was applied to the side of the sample and the copper post and cured at room temperature. Conduction between the top of the sample and the copper post was confirmed. Care was also taken to maximize the probability of a good cleaved surface. A pre-cut was made on the side of the sample using a surgical razor blade, parallel to the a-b face. This was to ensure cleaving at a designated location, rather than at inclusions and imperfections as would be the tendency without a pre-cut¹². This is one of the essential steps

that enabled successful ARPES measurements.

We studied nearly-optimally-doped Hg1201 ($T_c=95K$, determined at the transition midpoint). Data were taken at SSRL at 10K with a Scienta R4000 analyzer and 10 meV energy resolution. Samples were cleaved in-situ at a pressure better than 5×10^{-11} Torr.

Experiments were attempted with a 7eV laser, near 55 eV at beamline 10.0.1 of the Advanced Light Source (ALS), and near 19 eV at beamline 5-4 at Stanford Synchrotron Radiation Lightsource (SSRL). The latter experimental condition was found to yield the best spectra, and the quality of the measured spectra depended sensitively on the experimental conditions. Fig. 1(d) shows energy distribution curves (EDCs) at the Fermi crossing momentum, k_F , at the node taken with several photon energies between 18.6 and 19.6 eV. The amplitude of the quasiparticle peak relative to the background varies rapidly with the choice of photon energy, even within this narrow range. Quasiparticle peaks were clearly observed for 19-19.4 eV photon energy and very weak for 18.6, 18.8, and 19.6 eV photon energies. The nodal quasiparticle peak was found to be most pronounced for 19.4 eV photon energy and Γ -M cut geometry. For this cut geometry, the polarization of the beam at SSRL is 45° from the Cu-O bond direction. Note that because Hg-1201 is tetragonal, the M point is the Brillouin zone corner, and Γ -M cuts are along the $(0,0)-(\pi,\pi)$ line.

II. MOMENTUM DEPENDENCE

Using the optimal experimental configuration, electron states near the node are accessible, but the spectral intensity is very small at the antinode, likely because of extrinsic reasons. Fig. 2 shows momentum dependence of spectra. The band is most pronounced near the node in this experimental configuration, and spectral intensity diminishes away from the node. By $\theta=21^\circ$, quasiparticles are no longer observed. EDCs at k_F are shown in Fig. 2(h). All spectra have a strong energy-dependent background, shown in Fig. 2(f), which is identical for all cuts. Previous studies have suggested that this ARPES background is attributed to photoelectrons which scattered inside the sample and lost their momentum information prior to being photoemitted²³. In Hg1201, additional contribution to the background may come from photoelectrons scattering from surface step-edges. Subtracting this background EDC highlights the quasiparticle peaks, as shown in Fig. 2(i). Similar methods have been used to discern spectral features buried beneath a large background in other cuprates²⁴.

The apparent decrease of cross-section away from the node is likely not intrinsic, as most cuprates with comparable T_c show antinodal quasiparticles at optimal doping with proper experimental conditions²⁵⁻²⁷. Matrix element effects are generally one reason spectral intensity may be unobservable. In ARPES experiments, the measured spectral intensity is modulated by a dipole matrix

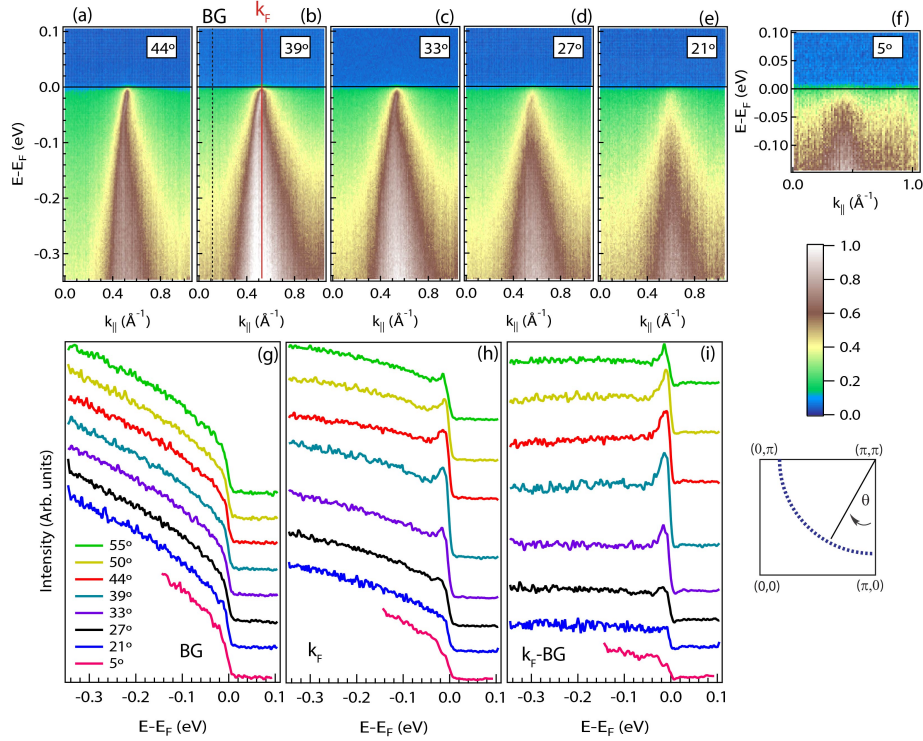


FIG. 2. (a)-(f) Image plots of near-nodal cuts. All images have the same linear color scale. Color scale and Fermi surface angle θ are defined below (f). Color scale is in arbitrary units. Data taken with 19eV photons, cuts parallel to ΓM , and $T=10K$. Red vertical line in (b) marks Fermi momentum (k_F) and black dashed line marks momentum of background EDC. (g) Background EDCs, taken at momentum indicated in (b). (h) EDC at k_F . (i) EDC at k_F with background EDC subtracted.

element term $|M|^2 = |\langle \Psi_f | \mathbf{A} \cdot \mathbf{p} | \Psi_i \rangle|^2$ where \mathbf{A} is the photon vector potential, \mathbf{p} is the electron momentum, and $\Psi_f(\Psi_i)$ are wavefunctions of the final (initial) electron states. Changes in the photon energy or polarization can affect the intensity of a band measured by ARPES and also which orbitals are highlighted^{28,29}. For cuts along high-symmetry directions in the Brillouin zone, certain light polarization can suppress a band in the ARPES spectrum based on its orbital character. Final-state effects can completely suppress a band in the ARPES spectrum if there are no final states to excite into with the chosen photon energy. Further exploration is needed to find an experimental configuration where the antinode has adequate cross section for Hg1201. We note that quasiparticles near the node are pronounced only within a limited range of photon energies (Fig. 1(d)), which is one of the reasons that ARPES data on Hg1201 were not available previously. Optimizing the experiment for the antinode will likely require similar careful exploration over parameter space—photon energy, polarization, cut geometry.

Fig. 3 shows a Fermi surface color map and k_F values for each cut. Data taken with 19 eV (experiment A) and 19.4 eV (Experiment B) photons yielded a similar Fermi surface. Data were taken on two opposite sides of the Γ point on both sides of the node. Four-fold rotational symmetry was assumed to fill the quadrants in which

data were not taken in the color plot, but symmetrization was not applied to k_F data (blue squares, red circles). Fig. 3 also shows tight binding Fermi surfaces for hole dopings $0.07 < p < 0.19$ with hopping parameters which provide the best fit to dispersions from first-principles calculations³⁰: $(t, t', t'', t''') = (0.46, -0.105, 0.08, -0.02)$.

The chemical potential was adjusted to compare to the Fermi-crossings data (red and blue symbols in Fig. 3). For experiment A, the Fermi surface encloses an area of 1.47 \AA^{-2} , which amounts to a hole doping of $11.9 \pm 1.2\%$, using $1+p=2A_{FS}/A_{BZ}$, where A_{FS} (A_{BZ}) is the area of the Fermi surface (Brillouin zone). Experiment B yielded a hole doping of $11.6 \pm 0.7\%$. A lattice constant of 3.876 \AA was used³¹. We note that the correspondence between nominal doping and FS area is much better than in as-cleaved $\text{YBa}_2\text{Cu}_3\text{O}_{7-\delta}$ (YBCO), another cuprate which lacks a neutral cleavage plane. In YBCO, a polar catastrophe is avoided by self-doping of the surface layer such that as-cleaved surfaces are very overdoped ($p \approx 0.3$)³², and in-situ surface dosing with potassium is required to produce optimally-doped and underdoped YBCO surfaces for ARPES study. The measured FS area in Hg1201 indicates that self-doping of the surface layer is less of an issue, which makes Hg1201 is a promising cuprate for comparing ARPES data to established bulk probes without the need for complex surface preparation.

Several caveats should be considered when interpret-

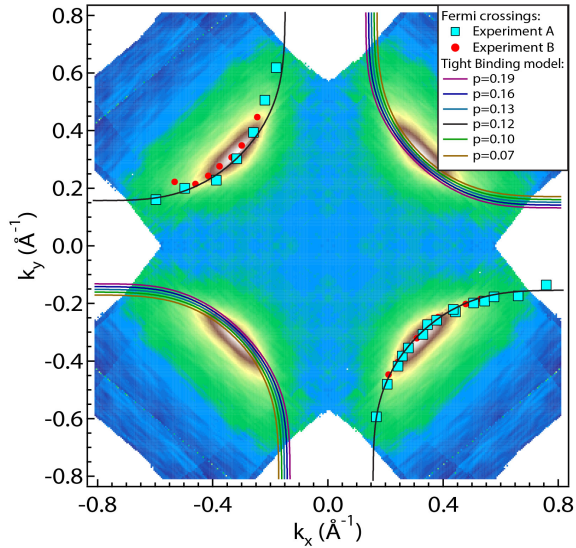


FIG. 3. Fermi surface map, k_F for each cut, and tight-binding model Fermi surfaces. Map is produced by integrating cuts within a 20 meV window centered at E_F . Four-fold symmetrization is applied to the color map, but not k_F data. Red and blue symbols are Fermi crossings for two different experiments on two different batches of crystals. For each cut, k_F was determined from the peak position of the momentum distribution curve at E_F . In the superconducting state, resolution effects produce finite intensity at E_F near the node from which this determination can be made. Experiment A was performed with 19eV photons and experiment B was performed with 19.4 eV photons. Solid lines are tight-binding Fermi surfaces enclosing different volumes, with hopping parameters from Ref. 30. For quadrants with k_F data, Fermi surfaces are only shown for $p=0.12$.

ing the Fermi surface volume in Fig. 3. First, there is uncertainty due to the lack of observed Fermi crossings in the antinodal region. The exact shape of the Fermi surface is not known because the antinodal segments have not been accessed experimentally. Second, the lack of a neutral cleavage plane may cause the hole concentration on the surface to be different from the bulk and perhaps to vary slightly between cleaves. It should also be noted that the agreement between Fermi surface area and nominal doping in the literature is mixed. In $\text{La}_{2-x}\text{Sr}_x\text{CuO}_4$ (LSCO), the Fermi surface area follows Luttinger's theorem, while in $\text{Ca}_{2-x}\text{Na}_x\text{CuO}_2\text{Cl}_2$ (Na-CCOC) and $\text{Bi}_2\text{Sr}_2\text{CuO}_{6+\delta}$ (Bi-2201), the FS area increases more rapidly with nominal doping^{33,34}. This has been associated with differences in how doping occurs in different cuprates. In LSCO, the chemical potential appears to be pinned inside the charge transfer gap, while in Na-CCOC and Bi-2201, the chemical potential shifts with doping. Finally, we note that thermoelectric power measurements of powder samples found a maximum T_c of 98K in Hg-1201 corresponding to 15.7% hole doping and a T_c of 95K corresponding to 12.7% hole doping³⁵, which is more consistent with our ARPES data. Future doping-dependent ARPES studies of the FS in Hg1201

can be expected to clarify the interpretation of the FS area observed in this experiment.

With a favorable experimental configuration, we were able to measure the momentum dependence of the superconducting gap in Hg1201 using ARPES, as shown in Fig. 4. Background EDCs were subtracted in order to emphasize the quasiparticle contribution for accurate extraction of the gap. E_F was determined from a polycrystalline gold sample which was electrically connected to the Hg1201 sample. Spectra were symmetrized and EDCs at k_f were fit to a minimal model convolved with the energy resolution of the experiment³⁶. Fitted gaps are plotted as a function of the simple d -wave form, $0.5|\cos(k_x) - \cos(k_y)|$. Extrapolating to the antinode, assuming the gap function obeys a simple d -wave form, gives an antinodal gap of 39 ± 2 meV. This is similar to the antinodal gap observed in Bi-2212 by ARPES at optimal doping^{37,38}, and also consistent with the doping-independent near-nodal gap slope observed in Bi-2212 $0.076 < p < 0.19$ ³⁸. This value of the superconducting gap (Δ) is furthermore consistent with the scaling between Δ and the magnetic resonance mode energy explored in Ref. 39. For Hg1201, Raman spectroscopy shows a peak in the B_{1G} channel corresponding to a 41 meV antinodal gap³, and tunneling experiments have reported a d -wave gap with a maximum of 33 meV⁴⁰.

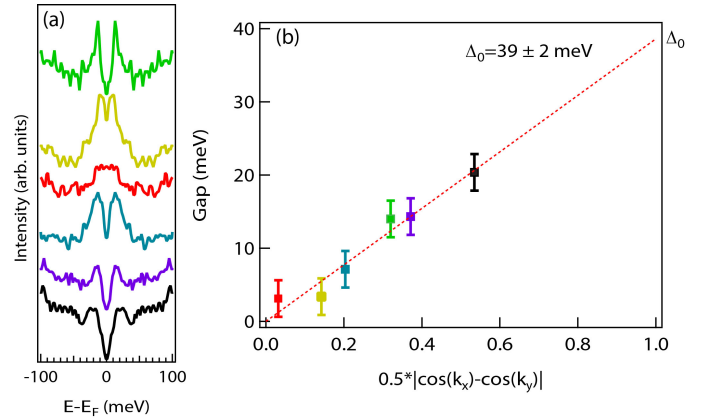


FIG. 4. Gap measurements, $T=10\text{K}$. (a) Symmetrized EDCs at k_F , using cuts in Fig. 2. Background EDCs (Fig. 2(g)) have been subtracted. EDCs are offset vertically. (b) Fitted gap at each momentum, plotted as a function of the simple d -wave form. Colors of EDCs in (a) correspond to colors of data points in (b) and to FS angles indicated in Fig. 2(g)-(i). Dotted line is linear fit, fixing y-intercept to zero.

III. NODAL DISPERSION ANALYSIS

Fig. 5 shows momentum distribution curves (MDCs) taken at the node. Selected MDCs are shown in panel (a), and they have certain peculiarities which were observed in every experiment on Hg1201. First, the MDCs near E_F deviate from a Lorentzian lineshape, with ex-

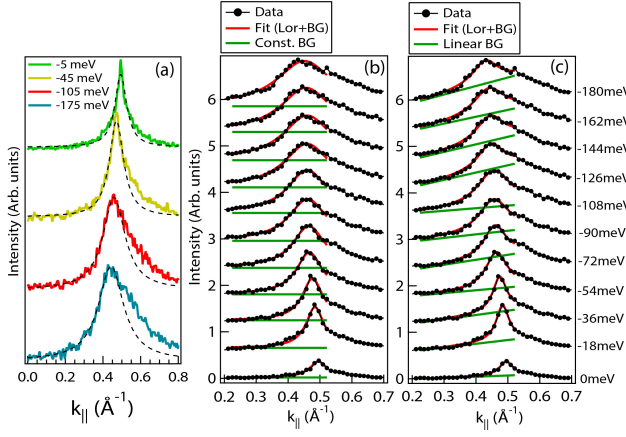


FIG. 5. MDCs at node. Data taken with 19.4eV photons. (a) Selected MDCs at indicated energies. Black dashed lines are Lorentzian fits to the left-hand side of each peak. (b)-(c) Fitting of MDCs separated by 18 meV in energy to a Lorentzian plus background (red curves). Green curves correspond to background, which is taken to be constant for (b) and linear (a+bk) for (c). The left and right limits of the red and green curves indicate the momentum range of the fit. Each MDC (black) is offset from the previous by 0.6 (arbitrary units).

tra weight in the tails, such that the peak height and width cannot be simultaneously captured. Moving to higher binding energy, the MDCs become increasingly asymmetric, with extra weight on the side of the peak further from the Γ point. Every sample studied showed the same asymmetry. The MDC asymmetry might reflect interesting physics, such as a momentum-dependent self energy due to correlation effects⁴¹. However, given the lack of a neutral cleavage plane, surface electric fields might be responsible⁴². Because of this MDC lineshape, using the usual fitting procedure of a Lorentzian peak plus a constant background does not yield the correct peak position at higher binding energy when asymmetry is strong (Fig. 5(b)). Using a linear background for each MDC better reproduces the peak position (Fig. 5(c)).

Fig. 6(b) shows MDC-derived dispersions at the node using both a constant (red) and constant+linear (blue) background. Both methods indicate dispersion anomalies near 50 meV and 200 meV, and they yield comparable low-energy dispersions (<50 meV). The former kink is ubiquitous in all cuprates, but the latter is slightly unusual because the high-energy anomaly is generally observed at higher binding energy in hole-doped cuprates⁴³. The lower energy kink will be the focus of the remainder of the discussion. Using a constant background yields steeper dispersions at higher binding energy, which is not physically correct because this fit does not capture the maximum of each MDC. The Fermi velocity (v_F) is found to be similar to other cuprates⁴⁴, disregarding a potential contribution from the very low energy kink ($\omega < 10$ meV) which is not accessible in this experiment⁴⁵. The velocity at higher energy (v_{HE} , 80-180 meV) is strongly dependent on the fitting scheme, with a constant back-

ground giving a slope that is 25% larger. This discrepancy can lead to an overestimation of the mass renormalization at the ≈ 50 meV kink. A linear background yields v_F (0-40 meV) = 2.008 ± 0.002 eV \AA and v_{HE} (80-180 meV) = 3.956 ± 0.064 eV \AA giving a mass enhancement factor $1 + \lambda \approx v_F/v_{HE} = 1.97 \pm 0.09$.

Many-body interactions in materials are captured in the self energy, $\Sigma(\omega) = \text{Re}\Sigma(\omega) + i\text{Im}\Sigma(\omega)$, where $\text{Re}\Sigma(\omega)$ and $\text{Im}\Sigma(\omega)$ describe interaction-induced corrections to the band dispersion and quasiparticle lifetime, respectively. Both quantities are available from ARPES data^{46,47}, and because $\text{Re}\Sigma(\omega)$ and $\text{Im}\Sigma(\omega)$ are Kramers-Kronig related, many-body effects show features in both quantities. Most analyses, including this one, assume that Σ is independent of k normal to the FS. Fig. 6(c) shows the real part of the self energy, $\text{Re}\Sigma$, at the node, approximated by subtracting an assumed linear bare band (blue dashed line in Fig. 6(b)) from the measured MDC dispersion (blue solid line). This quantity is peaked at 51 meV. The imaginary part of the self energy, $\text{Im}\Sigma$, is approximated by the MDC FWHM multiplied by the slope of the assumed bare band. $\text{Im}\Sigma$ shows an inflection point at a similar energy, affirming data quality and confirming a genuine many-body effect, electron-boson coupling, at that energy. There is a small upturn in $\text{Im}\Sigma$ near E_F , but this is within the error bars, and likely not significant. There was some sample-to-sample variation in the kink energy, with another good cleave showing a kink energy as high as 58 meV. Interestingly, analysis of optical conductivity data in Hg1201 yielded a bosonic "glue" energy between 50 and 60 meV, consistent with the energy of this kink⁴⁸. In Fig. 6(e)-(f), comparisons are made to Bi-2212 with a similar T_c (UD92, $p=0.14$). The magnitude of $\text{Re}\Sigma$ is smaller in Bi-2212, suggesting stronger electron-boson coupling in Hg1201. Additionally, the kink energy is larger in Bi-2212, with $\text{Re}\Sigma$ peaking at 66 meV. Fig. 4 indicates that the superconducting gap in Hg1201 is comparable to that in Bi-2212, which suggests that bosonic modes of different energy are responsible for the kinks in the two compounds. For further comparison, optimally doped Bi2201 ($T_c=33$ K, $\Delta=15$ meV) has multiple distinct contributions to the nodal kink, and the most prominent features appear at 70 meV and 41 meV⁴⁹.

The origin of the 50-80 meV nodal kink in cuprates is still a topic of debate with some explanations favoring a phononic origin^{50,51} and others favoring a magnetic origin^{52,53}. We will consider the former first. For optical phonons, the kink will appear at an energy $\Omega + \Delta$, where Ω is the phonon energy, because the electron-phonon coupling vertex is generally non-zero for momentum transfer $\mathbf{q} = \mathbf{k}_{\text{antinode}} - \mathbf{k}_{\text{node}}$ ^{51,54}. Thus, given a 39 meV extrapolated antinodal superconducting gap, the kink observed in Hg1201 between 50-58 meV implies an optical phonon between 11-19 meV. Ref. 9 shows in-plane optical phonon branches dispersing between 8 meV and 14 meV together with an enhanced calculated phonon density of states at similar energy. Additionally, Raman

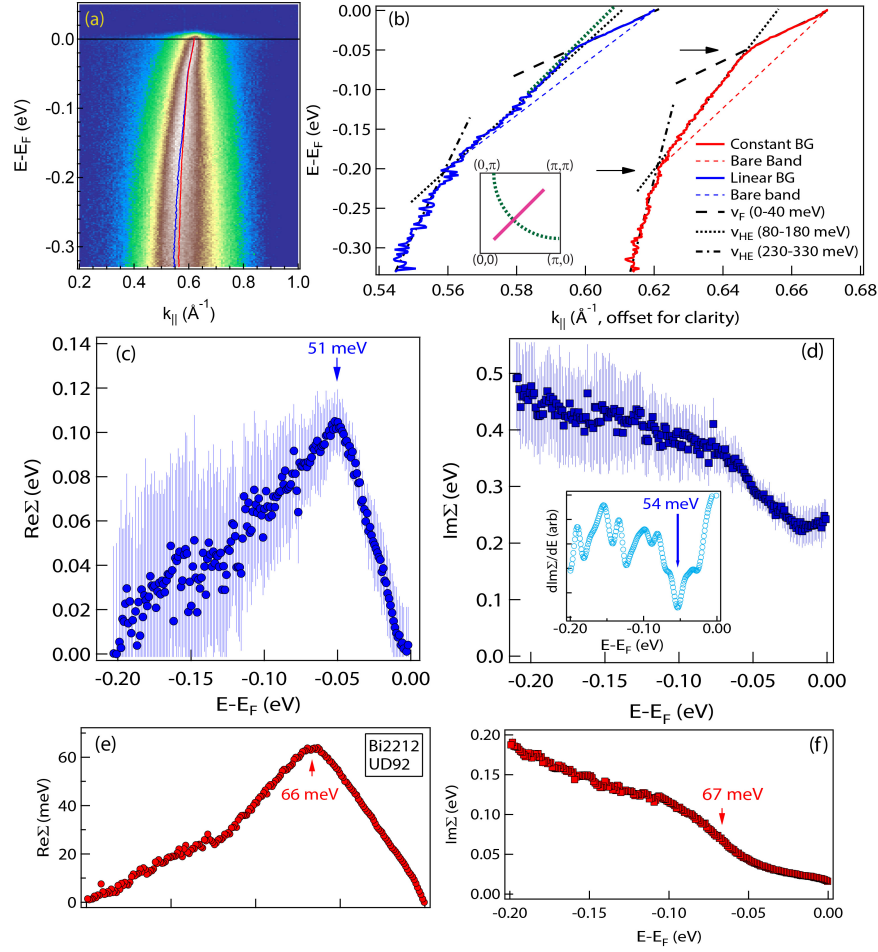


FIG. 6. (a)-(b) Nodal MDC analysis using constant (red) and linear (blue) background. (a) Image plot with MDC peak position from both fitting schemes. Background EDC has been subtracted from entire image. (b) MDC peak position dispersions, offset horizontally for clarity. Arrows mark key dispersion anomalies. Inset shows geometry for nodal cuts. (c) Real part of self energy, $\text{Re}\Sigma$, derived using bare band indicated in (b), as discussed in text. Linear-background fitting (Fig. 5(c)) was used. Arrow marks peak position. (d) Imaginary part of self energy, $\text{Im}\Sigma$. Inset: derivative $\text{Im}\Sigma$ (smoothed) with respect to energy. Arrow marks extremum. (e)-(f) $\text{Re}\Sigma$ and $\text{Im}\Sigma$ for Bi-2212 with $T_c=92\text{K}$ and $p=0.14$. Arrows mark peak of $\text{Re}\Sigma$ and inflection of FWHM. Bi-2212 data were taken at 10K and 3 meV energy resolution using 7eV photons and a SES2002 analyzer.

spectroscopy reports Raman-active phonons at 9 meV (Ba, E_g symmetry) and near 20 meV (Apical oxygen, E_g ; Ba, A_{1g})^{55,56}. These are potential candidates for the nodal kink in Hg1201, though we note that strong coupling to low-energy optical phonons is not supported by ARPES data on other cuprates. In Bi-2212, the nodal kink near 70 meV, is often attributed to an oxygen B_{1g} mode at ≈ 35 meV. The energy of this mode is inconsistent with the difference between the kink energy and gap energy in Hg1201, and additionally, single-layer cuprates are not expected to show electron-phonon coupling to first order for this mode⁵⁷. In Hg1201, the lack of a neutral cleavage plane and resultant surface electric fields presents an added complication. Surface electric fields could cause electrons near the surface to couple to phonons which are not Raman-active from symmetry arguments, and it could also affect the strength of electron-phonon coupling⁵⁷. Future information about

the precise surface termination from scanning tunneling microscopy could clarify how to interpret these data in terms of electron-phonon coupling.

Second, we explore the possibility of a magnetic origin of the kink in Hg1201. In neutron scattering, a magnetic collective mode has been observed below the pseudogap temperature ($T < T^*$), which disperses from 52 meV to 56 meV between $\mathbf{q}=(0,0)$ and $\mathbf{q}=(0.5,0.5)$ ⁸. This energy is intriguingly similar to the energy position of the nodal kink observed with ARPES. If the two phenomena are indeed related, it would imply that nodal electrons couple to this magnetic collective mode without effects due to the superconducting gap elsewhere in momentum space. This can happen if coupling is strongly peaked at $\mathbf{q}=0$ (forward scattering) or at a wavevector connecting two nodal points. Further doping, temperature, and momentum-dependent investigation is needed to clarify the origin of the nodal kink seen in Hg1201.

IV. CONCLUSIONS

Despite its lack of a natural cleavage plane, Hg1201 is a crucial compound to explore with ARPES because of its structural simplicity and the wealth of high-quality data obtained with other probes. The present work describes our technical experimental progress and measurement of basic electronic properties available in ARPES: superconducting gap, nodal kink energy, and band renormalization.

Future studies may be aided by a more controlled method to cleave the samples^{58,59}, by better control of the surface termination, and by finding experimental conditions where the antinode has adequate cross section. Experiments with higher photon energy ($h\nu > 100$ eV) may be promising to achieve the latter goal⁶⁰.

Ultimately, studies of Hg1201 may be very fruitful in addressing the question of 'what causes a high T_c ?' via comparisons to other single layer cuprates. A great body of ARPES studies exists for LSCO and Bi-2201, the 'low T_c ' single-layer cuprates^{33,46,61–63}. In contrast, there have been fewer ARPES studies on $\text{Ti}_2\text{Ba}_2\text{CuO}_{6+\delta}$

(Ti2201)^{27,64,65} and none on Hg1201 prior to the present work. Understanding the electronic structure of these 'high T_c ' single layer cuprates is crucial for discerning the ingredients for higher T_c . With comprehensive studies of Hg1201 and Ti2201, new and non-trivial features may be found in the electronic structure which distinguish the low T_c compounds from the high T_c ones.

ACKNOWLEDGMENTS

The authors acknowledge helpful discussions with Sri Raghu, Edbert Jarvis Sie, and Fahad Mahmood. SSRL is operated by the DOE Office of Basic Energy Science, Division of Chemical Science and Material Science. This work is supported by DOE Office of Science, Division of Materials Science, with contracts DE-FG03-01ER45929-A001 and DE-AC02-76SF00515. The work at the University of Minnesota was supported by the Department of Energy, Office of Basic Energy Sciences under Award No. de-sc0006858. N.B. acknowledges support through a Marie Curie Fellowship and European Research Council (Advanced Grant Quantum Puzzle, no. 227378).

* Current address: School of Pharmaceutical Engineering, Shenyang Pharmaceutical University, Shenyang, 110016, China

¹ N. Barišić, M. K. Chan, Y. Li, G. Yu, X. Zhao, M. Dressel, A. Smontara, and M. Greven, *Proceedings of the National Academy of Sciences* **110**, 12235 (2013).

² M. Le Tacon, A. Sacuto, A. Georges, G. Kotliar, Y. Gallais, D. Colson, and A. Forget, *Nature Physics* **2**, 537 (2006).

³ Y. Li, M. Le Tacon, M. Bakr, D. Terrade, D. Manske, R. Hackl, L. Ji, M. K. Chan, N. Barišić, X. Zhao, et al., *Phys. Rev. Lett.* **108**, 227003 (2012).

Y. Li, M. Le Tacon, Y. Matiks, A. V. Boris, T. Loew, C. T. Lin, L. Chen, M. K. Chan, C. Dorow, L. Ji, et al., *Phys. Rev. Lett.* **111**, 187001 (2013).

⁴ J. Bobroff, H. Alloul, P. Mendels, V. Viallet, J.-F. Marucco, and D. Colson, *Phys. Rev. Lett.* **78**, 3757 (1997).
D. Rybicki, J. Haase, M. Greven, G. Yu, Y. Li, Y. Cho, and X. Zhao, *Journal of superconductivity and novel magnetism* **22**, 179 (2009).

J. Haase, D. Rybicki, C. P. Slichter, M. Greven, G. Yu, Y. Li, and X. Zhao, *Phys. Rev. B* **85**, 104517 (2012).

⁵ M. S. Grbić, N. Barišić, A. Dulčić, I. Kupčić, Y. Li, X. Zhao, G. Yu, M. Dressel, M. Greven, and M. Požek, *Phys. Rev. B* **80**, 094511 (2009).

⁶ D. D. Xia, G. Yu, X. Zhao, B. Li, X. Liu, L. Ji, M. Chan, and M. Greven, *Superconductor Science and Technology* **25**, 115010 (2012).

⁷ F. Hardy, N. J. Hillier, C. Meingast, D. Colson, Y. Li, N. Barišić, G. Yu, X. Zhao, M. Greven, and J. S. Schilling, *Phys. Rev. Lett.* **105**, 167002 (2010).

S. Wang, J. Zhang, J. Yan, X.-J. Chen, V. Struzhkin, W. Tabis, N. Barišić, M. Chan, C. Dorow, X. Zhao, et al., *arXiv preprint arXiv:1310.0148* (2013).

⁸ Y. Li, V. Balédent, N. Barišić, Y. Cho, B. Fauqué, Y. Sidis,

G. Yu, X. Zhao, P. Bourges, and M. Greven, *Nature* **455**, 372 (2008).

Y. Li, V. Baledent, G. Yu, N. Barisic, K. Hradil, R. A. Mole, Y. Sidis, P. Steffens, X. Zhao, P. Bourges, et al., *Nature* **468**, 283 (2010).

G. Yu, Y. Li, E. M. Motoyama, X. Zhao, N. Barišić, Y. Cho, P. Bourges, K. Hradil, R. A. Mole, and M. Greven, *Phys. Rev. B* **81**, 064518 (2010).

Y. Li, V. Balédent, N. Barišić, Y. C. Cho, Y. Sidis, G. Yu, X. Zhao, P. Bourges, and M. Greven, *Phys. Rev. B* **84**, 224508 (2011).

Y. Li, N. Egetenmeyer, J. L. Gavilano, N. Barišić, and M. Greven, *Phys. Rev. B* **83**, 054507 (2011).

Y. Li, G. Yu, M. K. Chan, V. Balédent, Y. Li, N. Barišić, X. Zhao, K. Hradil, R. A. Mole, Y. Sidis, et al., *Nature Physics* **8**, 404 (2012).

⁹ M. d'Astuto, A. Mirone, P. Giura, D. Colson, A. Forget, and M. Krisch, *Journal of Physics: Condensed Matter* **15**, 8827 (2003).

¹⁰ L. Lu, G. Chabot-Couture, X. Zhao, J. N. Hancock, N. Kaneko, O. P. Vajk, G. Yu, S. Grenier, Y. J. Kim, D. Casa, et al., *Phys. Rev. Lett.* **95**, 217003 (2005).

¹¹ H. Eisaki, N. Kaneko, D. L. Feng, A. Damascelli, P. K. Mang, K. M. Shen, Z.-X. Shen, and M. Greven, *Physical Review B* **69**, 064512 (2004).

¹² N. Barišić, Y. Li, X. Zhao, Y.-C. Cho, G. Chabot-Couture, G. Yu, and M. Greven, *Phys. Rev. B* **78**, 054518 (2008).

¹³ E. van Heumen, R. Lortz, A. B. Kuzmenko, F. Carbone, D. van der Marel, X. Zhao, G. Yu, Y. Cho, N. Barisic, M. Greven, et al., *Phys. Rev. B* **75**, 054522 (2007).

¹⁴ S. I. Mirzaei, D. Stricker, J. N. Hancock, C. Berthod, A. Georges, E. Van Heumen, M. K. Chan, X. Zhao, Y. Li, M. Greven, et al., *Proceedings of the National Academy of Sciences* **110**, 5774 (2013).

- ¹⁵ N. Doiron-Leyraud, S. Lepault, O. Cyr-Choiniere, B. Vignolle, G. Grissonnanche, F. Laliberté, J. Chang, N. Barišić, M. Chan, L. Ji, et al., *Physical Review X* **3**, 021019 (2013).
- ¹⁶ N. Barišić, S. Badoux, M. K. Chan, C. Dorow, W. Tabis, B. Vignolle, G. Yu, J. Béard, X. Zhao, C. Proust, et al., *Nature Physics* **9**, 761764 (2013).
- ¹⁷ L. Gao, Y. Xue, F. Chen, Q. Xiong, R. Meng, D. Ramirez, C. Chu, J. Eggert, and H. Mao, *Physical Review B* **50**, 4260 (1994).
- ¹⁸ S. Raghu, R. Thomale, and T. H. Geballe, *Phys. Rev. B* **86**, 094506 (2012).
- ¹⁹ N. Nakagawa, H. Y. Hwang, and D. A. Muller, *Nature Materials* **5**, 204 (2006).
- ²⁰ U. Hubler, B. A. Hermann, H. P. Lang, J. Karpinski, and H.-J. Güntherodt, *Surface and Interface Analysis* **27**, 521 (1999).
- ²¹ Y. Li, *Unconventional Magnetic Order and Excitations in the Pseudogap Phase of Mercury Barium Copper Oxide* (PhD Thesis, Stanford University, 2010).
- ²² X. Zhao, G. Yu, Y.-C. Cho, G. Chabot-Couture, N. Barišić, P. Bourges, N. Kaneko, Y. Li, L. Lu, E. M. Motoyama, et al., *Advanced Materials* **18**, 32433247 (2006).
- ²³ A. Kaminski, S. Rosenkranz, H. M. Fretwell, J. Mesot, M. Randeria, J. C. Campuzano, M. R. Norman, Z. Z. Li, H. Raffy, T. Sato, et al., *Phys. Rev. B* **69**, 212509 (2004).
- ²⁴ M. Hashimoto, R.-H. He, I. M. Vishik, F. Schmitt, R. G. Moore, D. H. Lu, Y. Yoshida, H. Eisaki, Z. Hussain, T. P. Devereaux, et al., *Phys. Rev. B* **86**, 094504 (2012).
- ²⁵ D. H. Lu, D. L. Feng, N. P. Armitage, K. M. Shen, A. Damascelli, C. Kim, F. Ronning, Z.-X. Shen, D. A. Bonn, R. Liang, et al., *Phys. Rev. Lett.* **86**, 4370 (2001).
- ²⁶ I. M. Vishik, E. A. Nowadnick, W. S. Lee, Z.-X. Shen, B. Moritz, T. P. Devereaux, K. Tanaka, T. Sasagawa, and T. Fujii, *Nature Physics* **5**, 718 (2009).
- ²⁷ W. S. Lee, K. Tanaka, I. M. Vishik, D. H. Lu, R. G. Moore, H. Eisaki, A. Iyo, T. P. Devereaux, and Z. X. Shen, *Phys. Rev. Lett.* **103**, 067003 (2009).
- ²⁸ A. Bansil, R. S. Markiewicz, C. Kusko, M. Lindroos, and S. Sahrakorpi, *Journal of Physics and Chemistry of Solids* **65**, 1417 (2004).
- ²⁹ M. Lindroos, S. Sahrakorpi, and A. Bansil, *Phys. Rev. B* **65**, 054514 (2002).
- ³⁰ T. Das, *Phys. Rev. B* **86**, 054518 (2012).
- ³¹ J. Wagner, P. Radaelli, D. Hinks, J. Jorgensen, J. Mitchell, B. Dabrowski, G. Knapp, and M. Beno, *Physica C: Superconductivity* **210**, 447 (1993).
- ³² M. Hossain, J. Mottershead, D. Fournier, A. Bostwick, J. McChesney, E. Rotenberg, R. Liang, W. Hardy, G. Sawatzky, I. Elfimov, et al., *Nature physics* **4**, 527 (2008).
- ³³ M. Hashimoto, T. Yoshida, H. Yagi, M. Takizawa, A. Fujimori, M. Kubota, K. Ono, K. Tanaka, D. H. Lu, Z.-X. Shen, et al., *Phys. Rev. B* **77**, 094516 (2008).
- ³⁴ T. Yoshida, X. J. Zhou, K. Tanaka, W. L. Yang, Z. Hussain, Z.-X. Shen, A. Fujimori, S. Sahrakorpi, M. Lindroos, R. S. Markiewicz, et al., *Phys. Rev. B* **74**, 224510 (2006).
- ³⁵ A. Yamamoto, W.-Z. Hu, and S. Tajima, *Phys. Rev. B* **63**, 024504 (2000).
- ³⁶ M. R. Norman, M. Randeria, H. Ding, and J. C. Campuzano, *Phys. Rev. B* **57**, R11093 (1998).
- ³⁷ W. S. Lee, I. M. Vishik, K. Tanaka, D. H. Lu, T. Sasagawa, N. Nagaosa, T. P. Devereaux, Z. Hussain, and Z.-X. Shen, *Nature* **450**, 81 (2007).
- ³⁸ I. M. Vishik, M. Hashimoto, R.-H. He, W.-S. Lee, F. Schmitt, D. Lu, R. G. Moore, C. Zhang, W. Meevasana, T. Sasagawa, et al., *Proceedings of the National Academy of Sciences* **109**, 18332 (2012).
- ³⁹ G. Yu, Y. Li, E. Motoyama, and M. Greven, *Nature Physics* **5**, 873 (2009).
- ⁴⁰ J. Y. T. Wei, C. C. Tsuei, P. J. M. van Bentum, Q. Xiong, C. W. Chu, and M. K. Wu, *Phys. Rev. B* **57**, 3650 (1998).
- ⁴¹ V. Brouet, A. Nicolaou, M. Zacchigna, A. Taleb-Ibrahimi, P. Le Fèvre, and F. Bertran, *Journal of Electron Spectroscopy and Related Phenomena* **185**, 146 (2012).
- ⁴² E. D. Hansen, T. Miller, and T.-C. Chiang, *Phys. Rev. B* **55**, 1871 (1997).
- ⁴³ W. Meevasana, X. J. Zhou, S. Sahrakorpi, W. S. Lee, W. L. Yang, K. Tanaka, N. Mannella, T. Yoshida, D. H. Lu, Y. L. Chen, et al., *Phys. Rev. B* **75**, 174506 (2007).
- ⁴⁴ X. J. Zhou, T. Yoshida, A. Lanzara, P. V. Bogdanov, S. A. Kellar, K. M. Shen, W. L. Yang, F. Ronning, T. Sasagawa, T. Kakeshita, et al., *Nature* **423**, 398 (2003).
- ⁴⁵ I. M. Vishik, W. S. Lee, F. Schmitt, B. Moritz, T. Sasagawa, S. Uchida, K. Fujita, S. Ishida, C. Zhang, T. P. Devereaux, et al., *Phys. Rev. Lett.* **104**, 207002 (2010).
- ⁴⁶ A. Damascelli, Z. Hussain, and Z.-X. Shen, *Rev. Mod. Phys.* **75**, 473 (2003).
- ⁴⁷ A. A. Kordyuk, S. V. Borisenko, A. Koitzsch, J. Fink, M. Knupfer, and H. Berger, *Phys. Rev. B* **71**, 214513 (2005).
- ⁴⁸ E. van Heumen, E. Muhlethaler, A. B. Kuzmenko, H. Eisaki, W. Meevasana, M. Greven, and D. van der Marel, *Phys. Rev. B* **79**, 184512 (2009).
- ⁴⁹ T. Kondo, Y. Nakashima, W. Malaeb, Y. Ishida, Y. Hamaya, T. Takeuchi, and S. Shin, *Phys. Rev. Lett.* **110**, 217006 (2013).
- ⁵⁰ X. J. Zhou, J. Shi, T. Yoshida, T. Cuk, W. L. Yang, V. Brouet, J. Nakamura, N. Mannella, S. Komiya, Y. Ando, et al., *Phys. Rev. Lett.* **95**, 117001 (2005).
- ⁵¹ T. Devereaux, T. Cuk, Z.-X. Shen, and N. Nagaosa, *Phys. Rev. Lett.* **93**, 117004 (2004).
- ⁵² A. Kaminski, M. Randeria, J. C. Campuzano, M. R. Norman, H. Fretwell, J. Mesot, T. Sato, T. Takahashi, and K. Kadowaki, *Phys. Rev. Lett.* **86**, 1070 (2001).
- ⁵³ S. V. Borisenko, A. A. Kordyuk, T. K. Kim, A. Koitzsch, M. Knupfer, J. Fink, M. S. Golden, M. Eschrig, H. Berger, and R. Follath, *Phys. Rev. Lett.* **90**, 207001 (2003).
- ⁵⁴ A. W. Sandvik, D. J. Scalapino, and N. E. Bickers, *Phys. Rev. B* **69**, 094523 (2004).
- ⁵⁵ M. C. Krantz, C. Thomsen, H. Mattausch, and M. Cardona, *Phys. Rev. B* **50**, 1165 (1994).
- ⁵⁶ X. Zhou, M. Cardona, C. Chu, Q. Lin, S. Loureiro, and M. Marezio, *Physica C: Superconductivity* **270**, 193 (1996).
- ⁵⁷ S. Johnston, F. Vernay, B. Moritz, Z.-X. Shen, N. Nagaosa, J. Zaanen, and T. P. Devereaux, *Phys. Rev. B* **82**, 064513 (2010).
- ⁵⁸ T. Muro, Y. Kato, T. Kinoshita, and Y. Watanabe, *Review of Scientific Instruments* **81**, 043901 (2010).
- ⁵⁹ M. Mansson, T. Claesson, U. O. Karlsson, O. Tjernberg, S. Pailhes, J. Chang, J. Mesot, M. Shi, L. Patthey, N. Momono, et al., *Review of Scientific Instruments* **78**, 076103 (2007).
- ⁶⁰ H.-J. Noh, J. Jeong, J. Jeong, E.-J. Cho, S. B. Kim, K. Kim, B. I. Min, and H.-D. Kim, *Phys. Rev. Lett.* **102**, 256404 (2009).
- ⁶¹ M. Hashimoto, T. Yoshida, K. Tanaka, A. Fujimori,

- M. Okusawa, S. Wakimoto, K. Yamada, T. Kakeshita, H. Eisaki, and S. Uchida, Phys. Rev. B. **75**, 140503(R) (2007).
- ⁶² T. Yoshida, M. Hashimoto, S. Ideta, A. Fujimori, K. Tanaka, N. Mannella, Z. Hussain, Z.-X. Shen, M. Kubota, K. Ono, et al., Phys. Rev. Lett. **103**, 037004 (2009).
- ⁶³ T. Kondo, R. Khasanov, T. Takeuchi, J. Schmalian, and A. Kaminski, Nature **457**, 296 (2009).
- ⁶⁴ M. Platé, J. D. F. Mottershead, I. S. Elfimov, D. C. Peets, R. Liang, D. A. Bonn, W. N. Hardy, S. Chiuzbajian, M. Falub, M. Shi, et al., Phys. Rev. Lett. **95**, 077001 (2005).
- ⁶⁵ A. D. Palczewski, T. Kondo, R. Khasanov, N. N. Kolesnikov, A. V. Timonina, E. Rotenberg, T. Ohta, A. Bendounan, Y. Sassa, A. Fedorov, et al., Phys. Rev. B **78**, 054523 (2008).